Computational Materials Science 141 (2018) 269–281

Contents lists available at ScienceDirect

Computational Materials Science

journal homepage: www.elsevier.com/locate/commatsci

An automated procedure for geometry creation and finite element mesh generation: Application to explicit grain structure models and machining distortion

Timothy J. Barrett, Daniel J. Savage, Milan Ardeljan, Marko Knezevic *

Department of Mechanical Engineering, University of New Hampshire, Durham, NH 03824, USA

ARTICLE INFO

Article history:
Received 18 August 2017
Received in revised form 26 September 2017
Accepted 26 September 2017

Keywords:
Microstructure
Micromechanics
Finite elements
Residual stress
Machining distortion

ABSTRACT

Explicit grain structure models within finite element (FE) computational tools are essential for conducting crystal plasticity simulations to elucidate the three-dimensional (3D) topological effects of microstructural evolution on micromechanical fields during plastic deformation. Such full-field framework can predict not only texture evolution but also the development of intra- and inter-granular misorientation, grain shape, and grain boundary character distribution in polycrystalline metals. This paper develops an automated procedure for the geometry creation and FE mesh generation of explicit grain structures to facilitate full-field crystal plasticity modeling of complex shapes other than cuboids. The procedure consists of: (1) generation of a synthetic voxel-based microstructure of cuboidal shapes using the software called digital representation environment for the analysis of microstructure in 3D (DREAM.3D), (2) cutting of the model into a final shape by Boolean operations in Abaqus software, and (3) generation of volume FE mesh for the shaped polycrystalline aggregate using a custom-built toolset involving Patran software. Explicit grain structure FE models for micropillar compression and for microtube forming are created as examples. To further demonstrate the utility and robustness of the automated procedure for making multiple cuts while attaining the state of stress equilibrium after each cut, machining distortion of an Inconel 718 aircraft engine disk is modeled. The starting material for machining had a distribution of bulk residual stresses resulting from prior thermo-mechanical processing. Specifically, turning and broaching operations are carried out using the procedure. During machining, the disk distorts as material is removed, while bulk residual stress fields evolve to reach a new equilibrium. The disk distortion during the material removal is predicted using the developed automated procedure in Abaqus.

1. Introduction

Computational mechanics of polycrystalline materials often employs full-field calculations of mechanical fields. The term 'full-field' indicates that constituent grains explicitly interact with each other, while the micromechanical fields, defined in term of stress and strain, are equilibrated under the strain compatibility conditions in a discretized spatio-temporal domain. Since critical aspects of extreme material behavior such as void nucleation are governed primarily by local strain concentrations, knowledge of plasticity processes at grain scale is necessary for understanding and predicting material behavior. Starting from the work reported in [1], the finite element (FE) numerical method has been extensively used to solve for such fields, often with a sub-grain FE mesh resolution [2–13]. Under uniform macroscopic loading, these models reveal heterogeneous deformation because they account for the spatial distribution of grain size and shape of constituent grains and their inherent anisotropy and inter-granular interactions. A Green function method provides an alternative to FE when solving the field equations over a spatial domain [14]. The methodology was initially developed to calculate the effective and local mechanical response of composites [15] and later advanced to calculate the visco-plastic deformation of polycrystalline metals [16]. It relies on the efficient fast Fourier transform-based algorithms to solve the convolution integral representing stress equilibrium under the strain compatibility over a voxel-based microstructural cell, which is periodic and initially cubic or a rectangular parallelepiped (cuboidal). Such microstructure cells are primarily aimed at understanding behavior of a material. While computationally

* Corresponding author at: University of New Hampshire, Department of Mechanical Engineering, 33 Academic Way, Kingsbury Hall, W119, Durham, NH 03824, USA.
E-mail address: marko.knezevic@unh.edu (M. Knezevic).

https://doi.org/10.1016/j.commatsci.2017.09.048
0927-0256/

efficient [17–19], this methodology is at a disadvantage relative to the crystal plasticity FE (CPFE) methods because many applications of polycrystal plasticity are in the form of more complicated shapes, and requiring boundary conditions that are not periodic. Moreover, the grain boundaries are not present as continuous surfaces in these voxel-based microstructural cells. In contrast to full-field models, mean-field models calculate homogenized material response without accounting for any grain-to-grain interactions [20–32].

In early works, CPFE studies have ignored the morphology of grains [33–39]. In subsequent developments, simple geometries such as cuboids, rhombic dodecahedrons, and truncated octahedrons were used to represent grains in CPFE primarily because these constructs can be readily generated over a spatial domain representing a microstructure [40–42]. Because of their uniform and highly simplified grain morphology, compared to a real microstructure, these CPFE models were unable to accurately capture the inter-granular and intra-granular mechanical fields [43]. These early models were also unable to effectively represent the structure of grain boundaries. More recently, individual grains have been modeled using many finite elements [5,6,44–47]. These studies confirmed that the grain morphology plays a significant role in determining stress-strain heterogeneities.

Modeling the evolution of grain structure along with grain boundaries with plastic deformation is necessary for a more complete understanding of local and overall material response. To this end, FE models allow for grain boundary representation as discretized surfaces. A widely use methodology for voxel-based explicit grain structure generation is the Voronoi tessellation method along with various extensions [45,46,48–51]. However, polyhedral-shaped non-uniform grain shapes created by the Voronoi tessellation methods are often unrealistic because rules for the organization and geometrical constraints of the grains produced are not unique. In addition, the grain boundaries appear as coarse disordered polygons. To relax these limitations, DREAM.3D (the digital microstructure analysis environment in 3D) software has recently been developed by U.S. Air Force Research Laboratory and Blue Quartz [52,53]. The software is a result of the work conceived in [54]. While well suited for generating voxel-based grain structures in cuboidal shapes with surface mesh over grain boundaries, meshing of grain structures in 3D is yet to become a capability of the software. In recent work, we have developed and integrated a set of tools relying on the grain boundary surface mesh from DREAM.3D to create volume mesh of high quality over grains, ensuring the conformal conditions between constituent grains [55,56]. The conformal conditions between constituent grains means that neighboring grains share triangular elements at grain boundaries.

Experimental techniques have also been developed to acquire voxel-based grain structure data in 3D, which can be used as a direct input into CPFE simulations. An automated robotic serial sectioning device has been developed to capture 2D images for every slice at a high rate [57,58]. The 2D images are stacked and post-processed to form a 3D microstructure. The crystallographic information can be supplied from EBSD, which can be periodically performed by interrupting the automated robotic serial sectioning procedure. Another technique, known as focused ion beam electron backscattered diffraction (FIB-EBSD), uses the FIB to perform the serial sectioning and EBSD to create the crystallographic map for each section [59–64]. Finally, the most advanced technique for acquiring such data is *in-situ,* non-destructive near-field high-energy X-ray diffraction microscopy (nf HEDM) [65–69]. Data defining the state of grain structure, crystal lattice orientations, lattice strains and associated residual stresses, various defects such as voids, and even dislocation density acquired using these experiments can be used to initialize and critically verify full-field models.

Voxel-based microstructural data can also be obtained by numerical models such as phase field models [70], Potts (Monte-Carlo) grain growth models [71,72], and cellular automata recrystallization models [73,74].

While such measured and simulated voxel-based grain structures can directly represent the finite element mesh (e.g. every voxel is a brick element) utilized in a CPFE simulation [75,76], typically the data is further processed by smoothing the voxel description of grain boundaries using various interpolation methods. Such interpolation methods are conveniently available within DREAM.3D, which can produce triangular grain boundary surface mesh of appropriate size. Most importantly, the data is post-processed to reduce the number of discrete elements to a computationally manageable resolution.

As mentioned above, the grain size, shape, and crystallographic orientation strongly influence the local mechanical behavior of a material [77–79]. To capture heterogeneous deformation behavior of polycrystals, grain structures can be explicitly modeled using CPFE methods. This is particularly true in simulations of micro-forming processes such as forming of micro-tubes [80,81] and various micromechanical tests such as micro-pillar compression [49]. As a result, there is a demand for creating grain structures for various specimen geometries to facilitate accurate simulations.

This work develops an automated procedure for the geometry creation and subsequent mesh generation of complex shapes in 3D. An explicit grain structure FE model of a micro-pillar for compression and a micro-tube for microforming are created to demonstrate the utility of the procedure for subsequent CPFE modeling. To further demonstrate the robustness and utility of the procedure, machining distortion of an Inconel 718 aircraft engine disk is modeled [82,83]. Multiple cuts intrinsic to the machining process are performed in an automated manner while attaining the state of stress equilibrium after each cut under a clamped condition and in the unclamped i.e. free state of the disk after machining. Aircraft engine disks are typically forged followed by heat treatment and machining [82,83]. Thus, the starting material for machining had a distribution of bulk residual stresses resulting from prior thermo-mechanical processing. In general, local residual stresses can be induced during machining, but the bulk residual stresses remain primarily from prior processes [84–87]. The extent of cutting induced stresses depends on machining parameters such as feed rate, depth of cut, and cutting speed, which have major influence on the surface integrity of a machined part. The model developed here considers the residual stresses from prior thermo-mechanical processes, but not the cutting induced stresses. During machining, the workpiece distorts as material is removed, while bulk residual stress fields evolve to reach a new equilibrium. The comparisons between the measured distortion trends and the numerical predictions are presented and discussed. Good predictions demonstrate that the model is well suited for evaluating distortions during and after machining.

2. Automated procedure

Predictive capabilities of models such as CPFE are greatly improved by explicitly meshing grain structure and grain boundary surfaces. Creation of realistic grain structure models has been significantly advanced with the introduction of DREAM.3D [53]. This software, among other features, can generate 3D synthetic voxel-based microstructures and triangular surface mesh representing grain boundaries. The output of DREAM.3D in terms of the grain boundary surface mesh is a starting point for volume mesh generation. In recent work, we have developed an integrated toolset for volume meshing of grain structure models starting from the surface mesh [55]. However, the 3D grain structure models

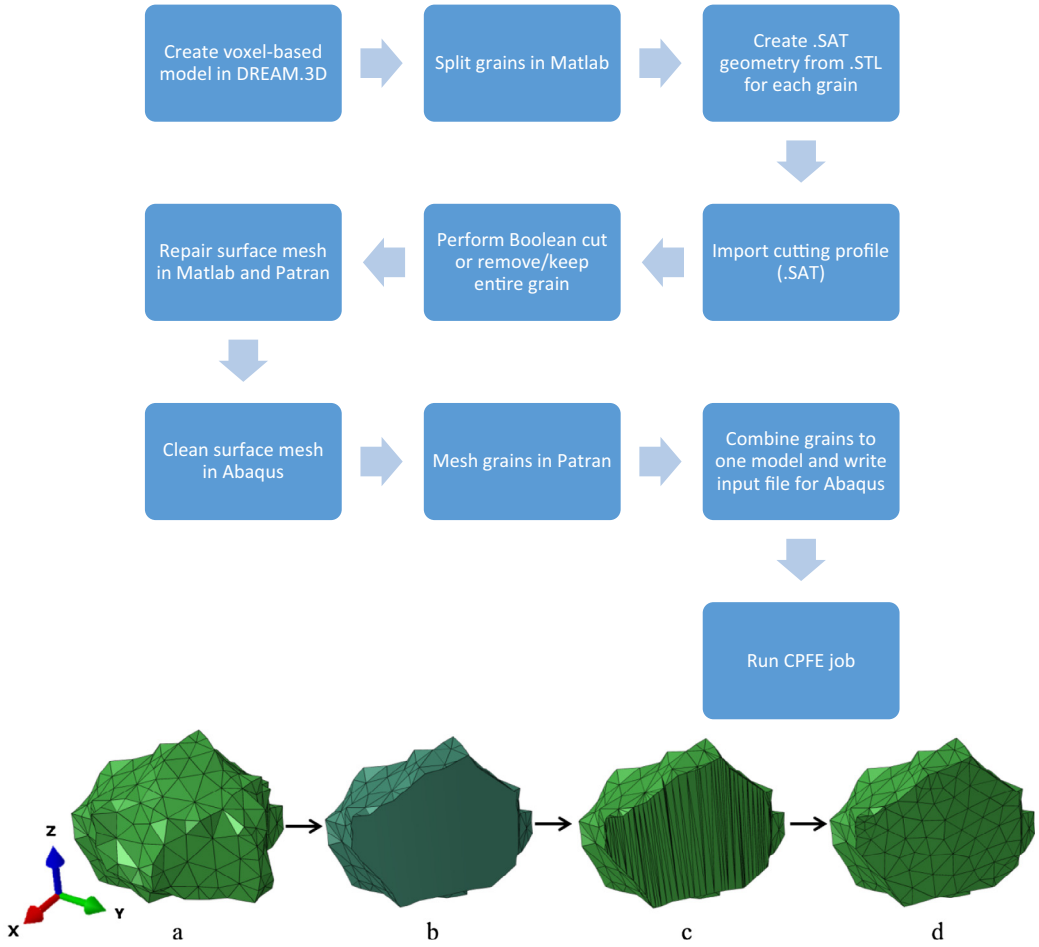

Fig. 1. Flowchart showing the overall steps involved in automated procedure for creating a grain structure FE model of a desired shape. The insert at bottom depicts the stages in the procedure explained using an arbitrary grain surface mesh: (a) surface mesh of the given grain generated in DREAM.3D represented in an .STL format (before the Boolean cut is performed), (b) grain geometry represented in an .SAT file format after the Boolean cut, (c) grain surface mesh saved as an .STL file after the Boolean cut, and (d) grain surface mesh after the mesh repair and cleaning procedure is performed in Matlab and Abaqus, respectively.

were always cuboids. Building on these prior efforts, we develop here a novel procedure for subtracting geometry from cuboidal grain structure to enable modeling of more complex shapes. The procedure is described next with specifics pertaining to a single Boolean cut from multiple objects/grains and multiple Boolean cuts from a single object/workpiece. We emphasize that the procedure is sufficiently general to facilitate performing multiple Boolean cuts from multiple objects and can further be extended to other geometric operations such as object merging.

2.1. Single Boolean cut from multiple objects (grains)

A synthetic voxel-based 3D microstructure of cubic shape is built using DREAM.3D for a given grain shape and grain size distribution. The output consists of a 3D voxelized model and a triangular surface mesh representing individual grain boundaries. Before obtaining the grain boundaries in the form of triangular surface mesh for each grain, it is convenient to apply a Laplacian based smoothing filter available in DREAM.3D. The filter smooths out and suppresses any jagged boundaries between grains to achieve better grain structure representation. These jagged grain boundaries represent imperfections resulting from the use of voxels. After this step, the 3D FE mesh of the polycrystalline aggregate can be generated using Patran [88]. A custom written Matlab script prepares the Patran meshing environment and run file, containing commands for individual grain surface mesh import, mesh size, 3D mesh generation, and 3D mesh export [55]. Linear tetrahedral finite elements (C3D4 – continuum 3D 4 nodes) are typically used for volume meshing from the individual grain surface meshes. Quadratic tetrahedral elements like C3D10 can alternatively be used. After the volume meshing is performed within Patran, the resulting grain mesh is further processed in the Matlab script to combine grains into a single FE model. The script eliminates any duplicate nodes, which are present between two neighboring grains and writes an Abaqus input file [89]. The file contains the 3D mesh with conformal boundaries between grains and the related element sets needed to identify each grain.

The procedure described above can create an arbitrary cuboidal shaped explicit grain structure FE model, which can subsequently be cut into the desired geometry. Fig. 1 shows a flowchart of steps involved in removing a portion of a cuboid to create a FE grain structure model of a prescribed/desired shape. The procedure is automated and executed using the Matlab script outlined above. Notably, the script is extended to interface with Python scripting capabilities in Abaqus, which is used to perform Boolean geometry removal on the initial grain structure model. The Boolean cut operation is a function available in Abaqus facilitating removal of a predefined intersection between a cutting geometry profile and a given geometry that is being cut in 3D space. The geometries must have geometry associated with them i.e. must be defined in a geometry format such as the .SAT format. A geometry representing the cutting profile can be sketched using the drawing tools in the

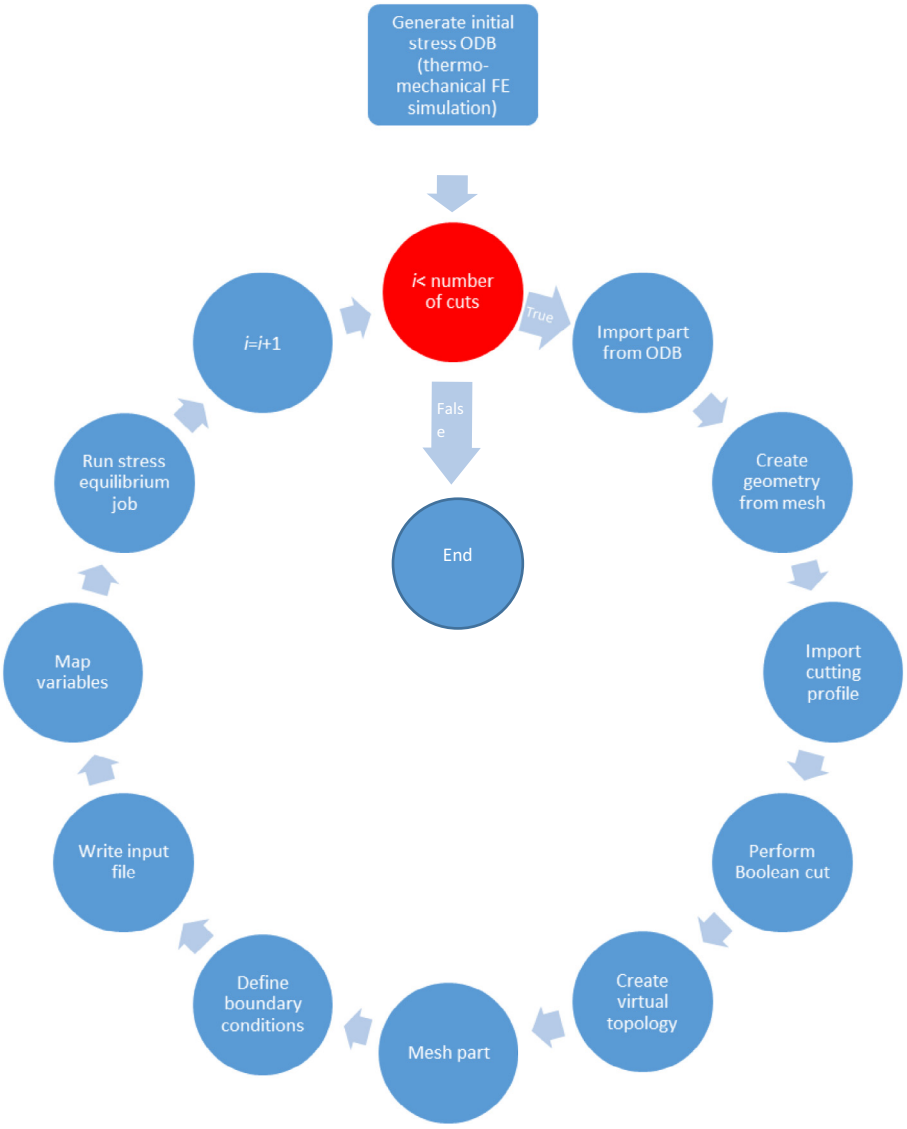

Fig. 2. Flowchart showing the overall steps involved in multiple cuts procedure. *i* indicates the current cut. ODB stands for Abaqus database file.

Abaqus part module or imported from a another software package for geometry creation, which enables the definition of more complicated geometry.

To begin, grains from DREAM.3D are separated within the Matlab script. Surface mesh of each individual grain is imported into Abaqus as an .STL file, which is subsequently converted into the necessary solid geometry (.SAT) to perform a Boolean cut operation based on a pre-defined cutting profile. The conversion of surface mesh into solid geometry is performed by "create geometry from mesh" Abaqus plugin, which assigns volume to its interior. At this point a Boolean cut is performed. After the cut is made, part of the geometry for each grain outside the cutting profile is kept and exported in the binary .STL format. It should be noted that not every grain undergoes cutting. Grains belonging with their entire volume to the cutting profile geometry are removed without cutting. In contrast, grains belonging with their entire volume to the final model geometry are included as intact. Surface meshes of all grains that were intersected with the cutting profile are additionally processed one-by-one in the Matlab script relying on Patran for surface meshing. These steps are shown in Fig. 1a-d for a randomly selected grain. The intersection contour line between the grain surface mesh and the cut may require additional seeding and/or removal of unnecessary nodes to ensure uniformity of nodal spacing (Fig. 1c and d). Subsequently, the interior of the cut surface is meshed in Patran starting from the seed on the intersection contour line. Afterwards, the control is returned to Matlab for assembling the entire surface mesh of all grains and writing an input file for Abaqus containing the entire surface mesh. In Abaqus, an additional cleanup is used to collapse triangular elements with poor aspect ratios. If any, these specific finite elements are always located at surfaces that underwent cutting. Notably, this Abaqus mesh cleanup procedure is done over the surface mesh of the entire model to ensure the overall mesh quality. The Matlab script then continues to prepare Patran meshing environment, to execute the Patran script for 3D volume meshing from individual grain surface meshes for each grain, to combine grains into one model removing duplicate nodes and to write the final Abaqus input file at the end of the procedure.

2.2. Multiple Boolean cuts from a single object (workpiece)

We now turn our attention to a procedure involving multiple Boolean operations, which is relevant to machining in which a number of cutting operations are usually performed. Although

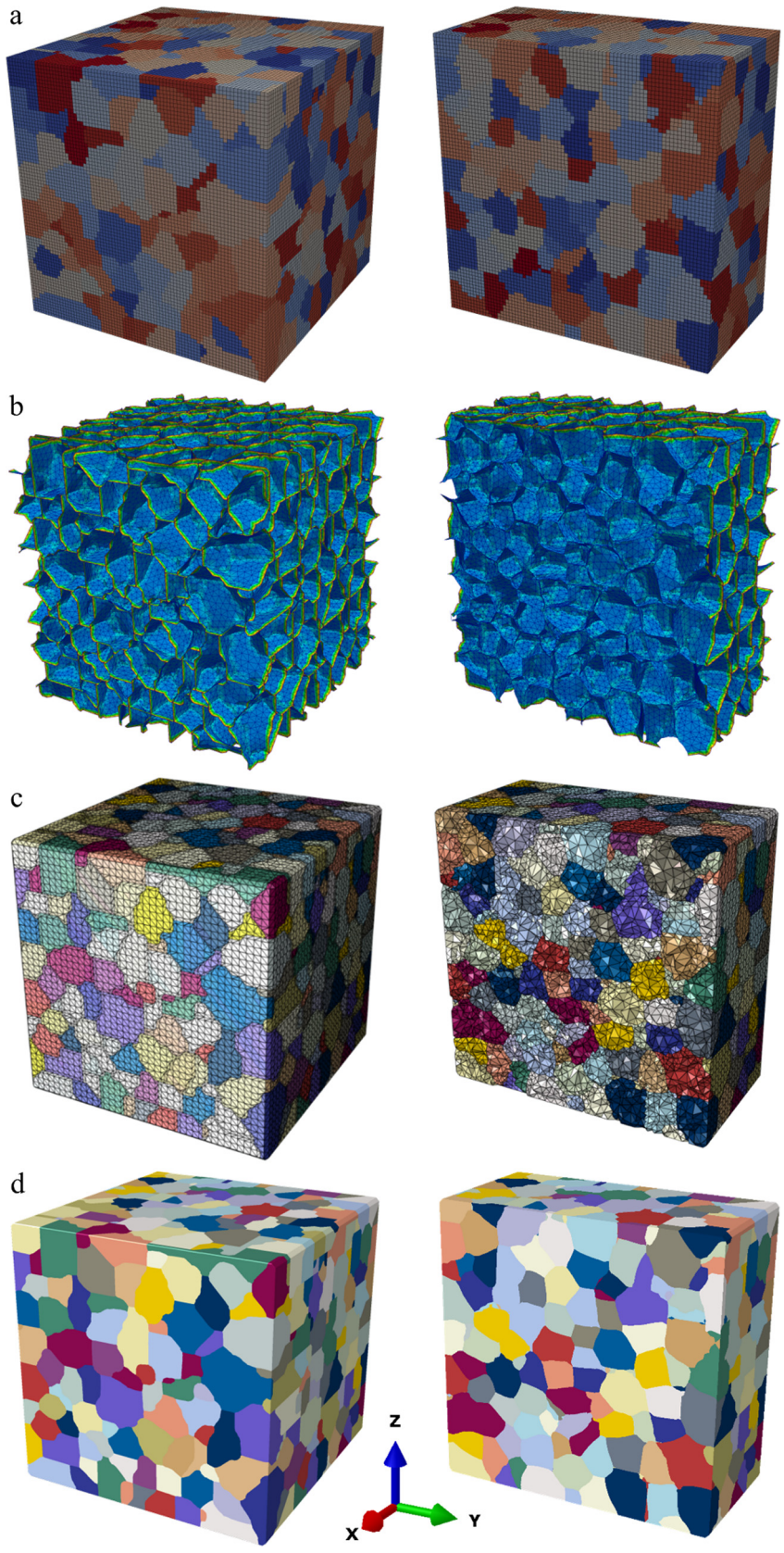

Fig. 3. An explicit grain structure model consisting of 784 equiaxed grains generated synthetically using DREAM.3D: (a) voxel-based model with highlighted edges, (b) triangular surface mesh, (c) finite element-based model, and (d) finite element-based model but without element edges. The edge length of the cube is 1000 μm, average grain size is 135 μm, and the total number of tetrahedral elements (type C3D4 or C3D10 in ABAQUS) in (c) is approximately 1,000,000. The mid-section along half x-axis shows the internal structure. Note that the triangular surface mesh in (b) describes grain boundaries.

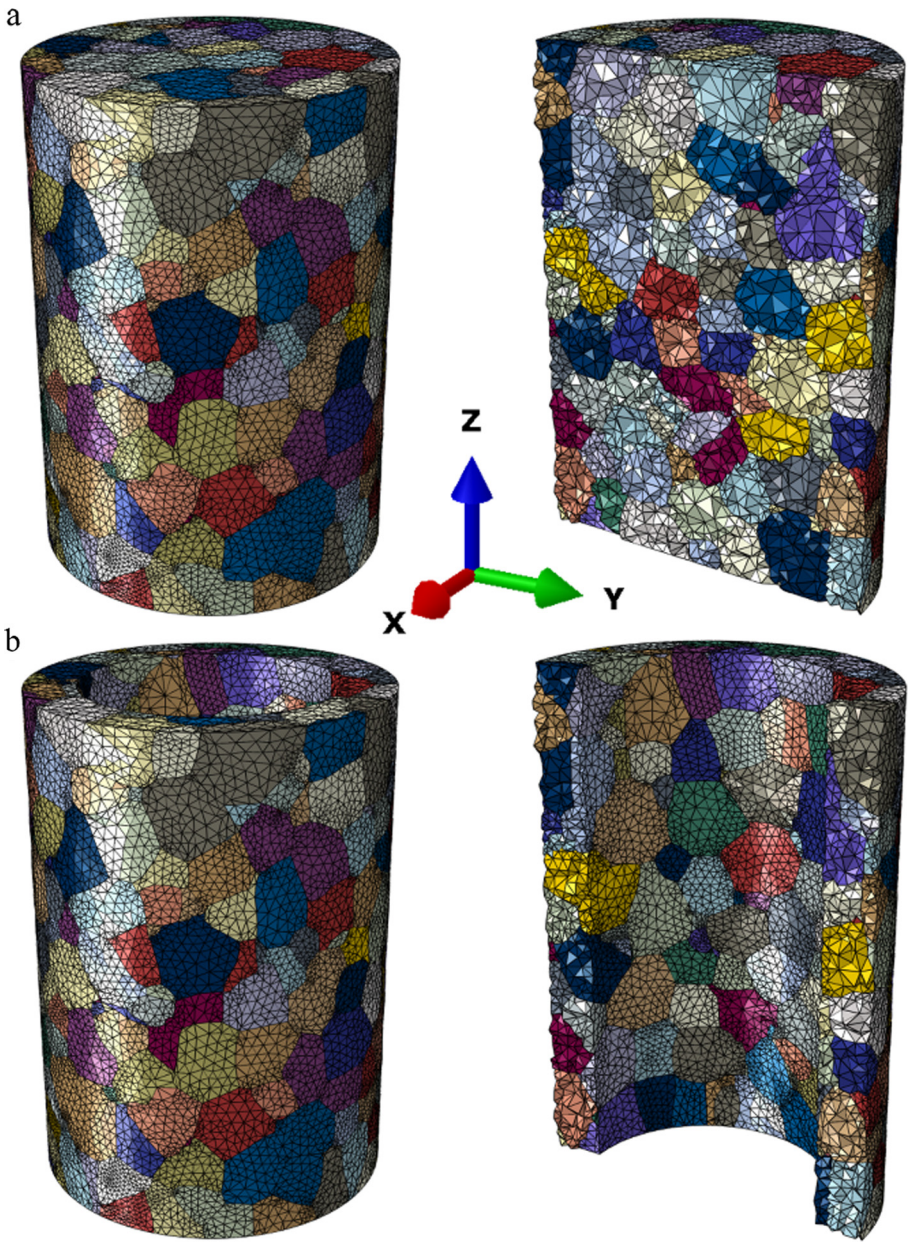

Fig. 4. Finite element explicit grain structure models machined from the model in Fig. 1: (a) a micropillar compression specimen consisting of 435 grains and 428,000 elements and (b) a microtube consisting of 366 grains and 276,000 elements. The outer and inner diameters are 700 μm and 500 μm, respectively, while the height is 1000 μm. The mid-sections along half x-axis show the internal structure.

the procedure is conceived as generic, for cutting a single object or a grain structure consisting of many objects or grains, we focus on machining distortion driven by residual stresses in a single object/-workpiece as a case study. Fig. 2 shows the flow of the procedure. The simulations are performed iteratively for every cut using the Python Abaqus scripting interface. In the absence of a grain structure model, Matlab and Patran are not needed and the entire procedure can be performed in the Abaqus framework.

During thermo-mechanical processing, a part continuously deforms as temperature and mechanical fields evolve because the stress equilibrium must be satisfied at any instance. The material removal procedure begins from a database (.ODB) containing a thermo-mechanically processed part with a residual stress field. During subsequent machining, Boolean operations are used for material removal in order to produce a machined part of required geometry. The machining distortion due to the redistribution of bulk residual stress is simulated in a fully automated manner as follows.

A deformed workpiece is imported from an .ODB file as an orphan mesh. The orphan mesh is converted into geometry using the "create geometry from mesh" plugin as was used for converting .STL files of grains. Subsequently, a cutting profile (volume-to-be-removed) is imported from a .SAT file. A Boolean cut subtracts the volume-to-be-removed from the geometry of the workpiece. Virtual topology tools are then used to remove any small faces, small edges, and skewed features from the cut workpiece, but not changing the actual geometry. Note that virtual topology was not used in cutting the complex granular geometries because a more sophisticated procedure was necessary for handling the cut surfaces and compatibility of grain boundaries, as described earlier. The cut part is seeded locally to the cut and then globally allowing the part to be meshed using a predefined mesh density

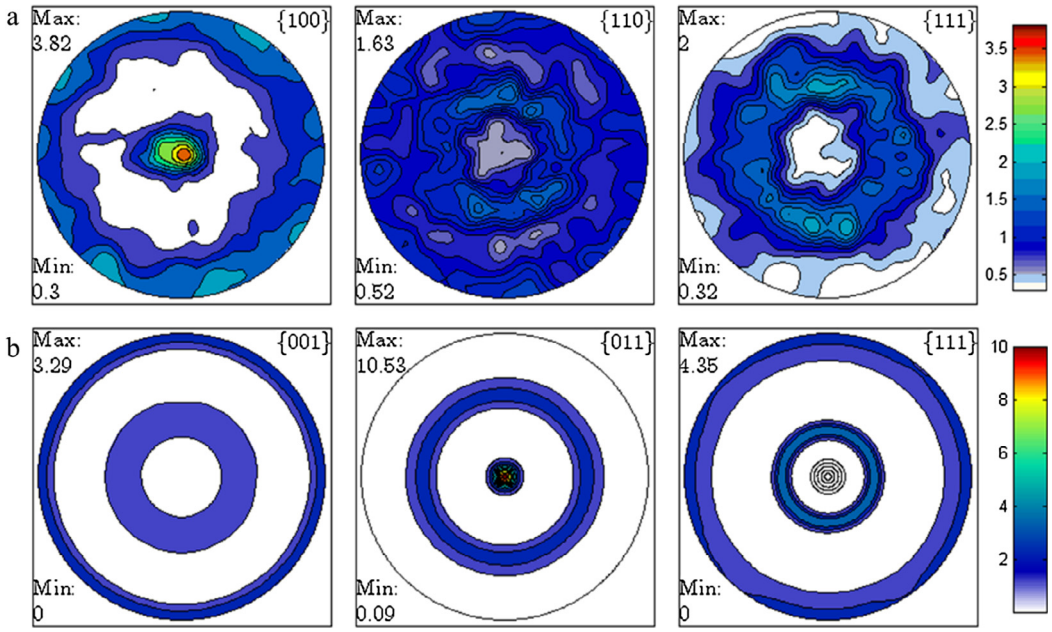

Fig. 5. Stereographic pole figures showing (a) {0 0 1} and (b) {0 1 1} fiber initial textures used in calculating the elastic stiffness tensor for the anisotropic elasticity calculations. The former textures were taken from [90], where IN718 was manufactured by direct metal laser sintering. The deposition direction is in the center of the pole figures (Z-axis). The latter texture was created by simple compression of a random initial texture represented using 4096 crystal orientations to a strain of 1.9. The compression axis is in the center of the pole figures (Z-axis).

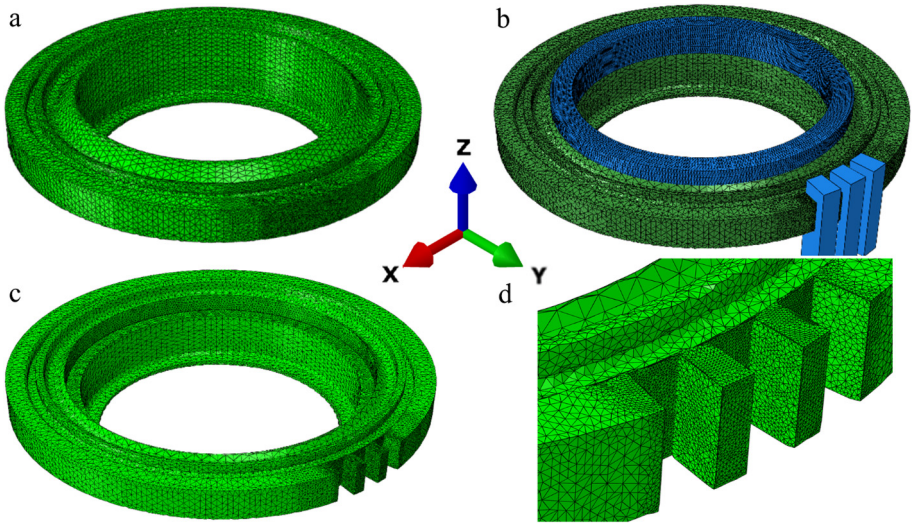

Fig. 6. (a) Initial FE model consisting of approximately 200,000 C3D4 elements. (b) Setup showing the slots and ring geometry to be removed by Boolean operations. (c) FE model after material removal. (d) Zoom into the refined mesh after the slots removal.

and element type. The stress and any other necessary state variables are mapped from the old mesh (before material removal) to the new mesh (after material removal) using the Abaqus function MAP SOLUTION. Mapping a solution from one mesh to another is always a step after remeshing, which transfers solution variables from an old mesh to a new mesh that occupies the same space. The MAP SOLUTION flag is placed in the input file and right before running the job, we reference the old job from which the stress is mapped from. To minimize the mapping error, the mesh not effected by the cut is preserved as much as possible. This is achieved serendipitously through topology artifacts generated in the orphan mesh to geometry procedure.

The Boolean cut is performed under a given boundary condition representing the clamping of the part by various fixtures during machining. The fixtures can be defined as separate objects or using bounding boxes selecting nodes where the part is clamped by applying pressure. In practice, different cutting tools and fixtures may be introduced between operations during the machining of a part. Finally, Abaqus input file is written and the job is run for stress equilibrium. The simulation framework developed here facilitates carrying out multiple passes and operations automatically starting from an initial workpiece with a bulk stress distribution and ending with a final machined geometry. Within one operation (or one set of fixtures), Boolean cut, meshing, interpolation, and stress equilibrium are carried out for each machining pass. Note that multiple machining passes can be simulated within a given operation. After every pass, the stress field in the workpiece reaches equilibrium, leading to a distortion in a clamped state. Additionally, part distortion in free state i.e. after removing the clamping boundary conditions can be simulated. This is when

the part is moved from one (e.g. a turning) to another (e.g. a broaching) operation or at the end of machining. Since none of the mapping and remeshing is necessary, the free state equilibrium is run as an additionally step after cutting. This means that the part is never imported from the ODB, there is no new input file written, and the stress is not mapped. The boundary conditions consist of only eliminating three translations and three rotations of the part, which is conveniently accomplished by constraining four nodes. The boundary conditions are automatically prescribed by the script.

The modeling procedure is applied to modeling of the machining distortion of an engine disk. Results and their validation are presented in the next section.

3. Results and discussion

This section presents case studies for generating shaped grain structure FE models and machining distortion.

3.1. Explicit grain structure model generation

A synthetic microstructure in 3D of cubic shape with edges of 1000 μm was built using DREAM.3D for a given average grain size of 135 μm and equiaxed grain shape (Fig. 3a). The generated voxel-based model contained an 80 × 80 × 80 voxel grid, where the edge of each 3D voxel was 12.5 μm in length. Length of the voxel edge influences surface mesh element size because the procedure for the conversion from a voxel representation and associated stair-stepped grain boundaries to the smooth triangular mesh grain boundaries in DREAM.3D is dependent on the starting voxel edge length. The smaller the starting voxel edge length, the finer the resulting grain boundary surface mesh. The voxel length of 12.5 μm is appropriately selected to obtain surface element size, which would result in a volume mesh of about 1,000,000 finite elements. Fig. 3b shows the surface mesh. The final granular microstructure consists of 784 grains. The final polycrystalline aggregate is comprised of element sets representing individual grains (Fig. 3c and d). The same initial lattice orientation can be assigned to all finite elements in an element set representing a grain in the user material subroutine.

Explicit grain structure FE models of a micropillar for compression and a microtube for microforming shown in Fig. 4 are created from the model in Fig. 3 using the single cut procedure described in Section 2.1. Inner and outer diameter were 700 μm and 500 μm respectively, while the total length of the models in the Z-direction remained 1000 μm. The cylinder model consists of 435 grains and a total of 428,000 finite elements, while the tube model contains 366 grains and 276,000 finite elements.

3.2. Machining distortion

For demonstration purposes, the automated modeling procedure involving multiple cuts is applied here to modeling of the machining distortion of an engine disk according to the data presented in [83].

3.2.1. Material

The disk is made of a Ni-based superalloy Inconel 718 (IN718). The only relevant material property for the distortion simulations is the elastic stiffness tensor. We performed isotropic and anisotropic elasticity simulations. For the latter, we considered {0 0 1} and {0 1 1} fiber textures (Fig. 5). The former texture forms during additive manufacturing of IN718 and is experimentally measured [90–92] while the latter forms during cylinder upsetting, which is more relevant for the present study since the disk is upset forged. It was synthetically created by simple compression of a random initial texture represented using 4096 crystal orientations to a strain of 1.9. Given a crystal orientation and single crystal elastic constants, the corresponding stiffness components of the local elastic stiffness tensor can be calculated using [93–97]

$$C_{abcd}(g) = C_{12}\delta_{ab}\delta_{cd} + C_{44}(\delta_{ac}\delta_{bd} + \delta_{ad}\delta_{bc}) + (C_{11} - C_{12} - 2C_{44})\sum_{n=1}^{3} g_{an}g_{bn}g_{cn}g_{dn}, \quad (1)$$

where g_{an} are the components of an orthogonal coordinate transformation matrix relating the crystal reference frame to the sample reference frame, and C_{11}, C_{12}, and C_{44} are the single crystal elastic constants of a cubic crystal. The macroscopic elastic stiffness was calculated as the volume average of the single crystal stiffness values [93,94]. The single crystal elastic constants for IN718 needed for the elastic stiffness tensor calculations of {0 0 1} and {0 1 1} fiber textures were: $C_{11} = 242,180$ MPa, $C_{12} = 138,850$ MPa, and $C_{44} = 104,200$ MPa [98], while Young's modulus and Poisson's ratio for the isotropic material were: 200,000 MPa and 0.3, respectively [90,99]. The values of the tensor components are presented in Appendix A.

3.2.2. Simulation setup

Simulation of hot upset forging and subsequent cooling created the residual stress distribution in a disk that was mapped onto a 3D mesh, which is used as an initial condition in the machining distortion analysis. The initial geometry and machining setup were

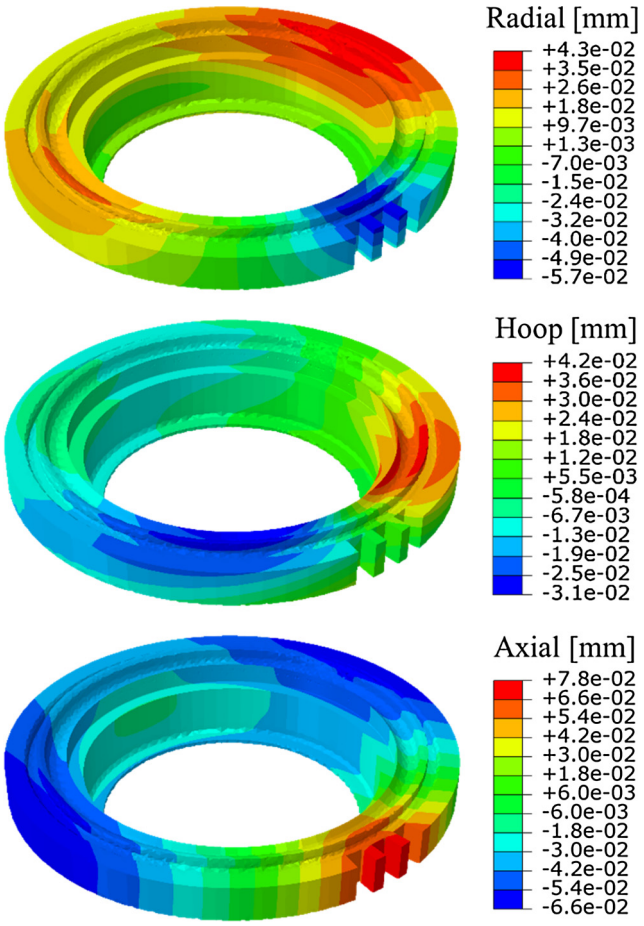

Fig. 7. Contours showing the displacement field increment from before to after the last turning operation in the free state of the disk for the isotropic simulation case. The disk is in the same frame as in Fig. 6.

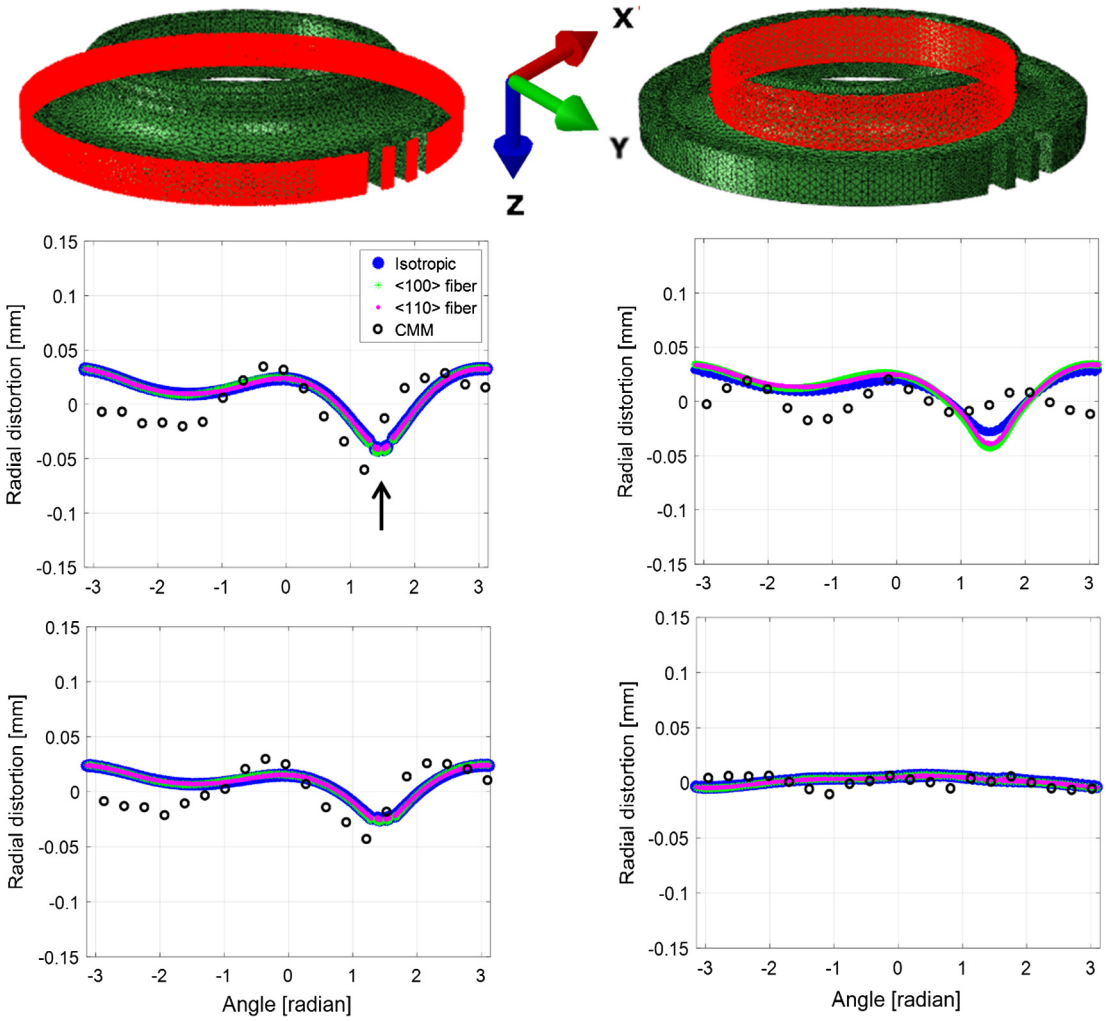

Fig. 8. Comparison of CMM (discrete symbols) measurements and predicted radial distortion for outer (on the left) and inner (on the right) diameter surfaces at two vertical locations: close to the top along the Z direction (upper plots) and close to the bottom (lower plots) of the disk. The highlighted nodes show the inspected surfaces by CMM, where the measurements are recorded at 20 points i.e. every 18° circumferentially for a given Z coordinate. The arrow points to the center slot.

presented and described in detail in [83]. For demonstration of the developed procedure for machining distortion, two machining operations are carried out here to obtain the machined geometry. The first one is broaching of three slots, and the second one is turning. Fig. 6a shows the initial mesh of the disk, while Fig. 6b shows the geometries of the slots to be removed by broaching and the ring to be removed by turning. To reduce the error introduced during mapping of state variables, a finer mesh was generated near the slots.

For the first operation, the disk was clamped axially from the top at four locations by the force from chucks, while the locating face was on the opposite side. The nodes belonging to the locating faces were fixed. The setup was presented in [83]. The three slots were removed in three separate passes. Every cut was followed by remeshing, interpolation, and stress equilibrium. At the end of the first operation, the unclamped stress equilibrium was obtained.

For the second operation, the disk was clamped radially by three chuck jaws, which were 120° apart. The chuck jaws applied force to the outer diameter surface, while the locating face was on the bottom side of the disk. The setup was presented in [83]. A Boolean cut was used to remove the ring followed by remeshing, interpolation, and stress equilibrium. Finally, the unclamped stress equilibrium was performed. Fig. 6c shows the disk after machining.

3.2.3. Numerical predictions

The approach to machining distortion developed in this work assumes that bulk residual stresses drive a part to distort as the material is removed. Fig. 7 shows the predicted incremental displacement in cylindrical coordinates of the disk caused by the last turning operation at the free state of the disk. To simulate the incremental displacement, the displacement field was initialized to zero before the second operation. While obtaining the cumulative distortion from multiple operations is straightforward, we present the last increment to facilitate the comparison with available experiments [83]. As the stress reaches equilibrium for the machined configuration, the disk becomes out-of-round in the radial direction, the slots tend to close in the hoop direction causing the disk to distort, and the disk warps in the axial direction. In the radial direction, the disk expands approximately ±90° from the slots. In the hoop direction, the disk is in compression, and so the slots tend to close. In the axial direction, the disk distorts downward approximately 90° from the slots but upward at the slots.

Coordinate measuring machine (CMM) measurements were used to evaluate trends of the FE predictions. The CMM measurement results were presented in [83] and used here (the measurements after the broaching operation and after the final turning operation). Fig. 8 shows a comparison between predicted and measured radial distortion (the increment in distortion from before and

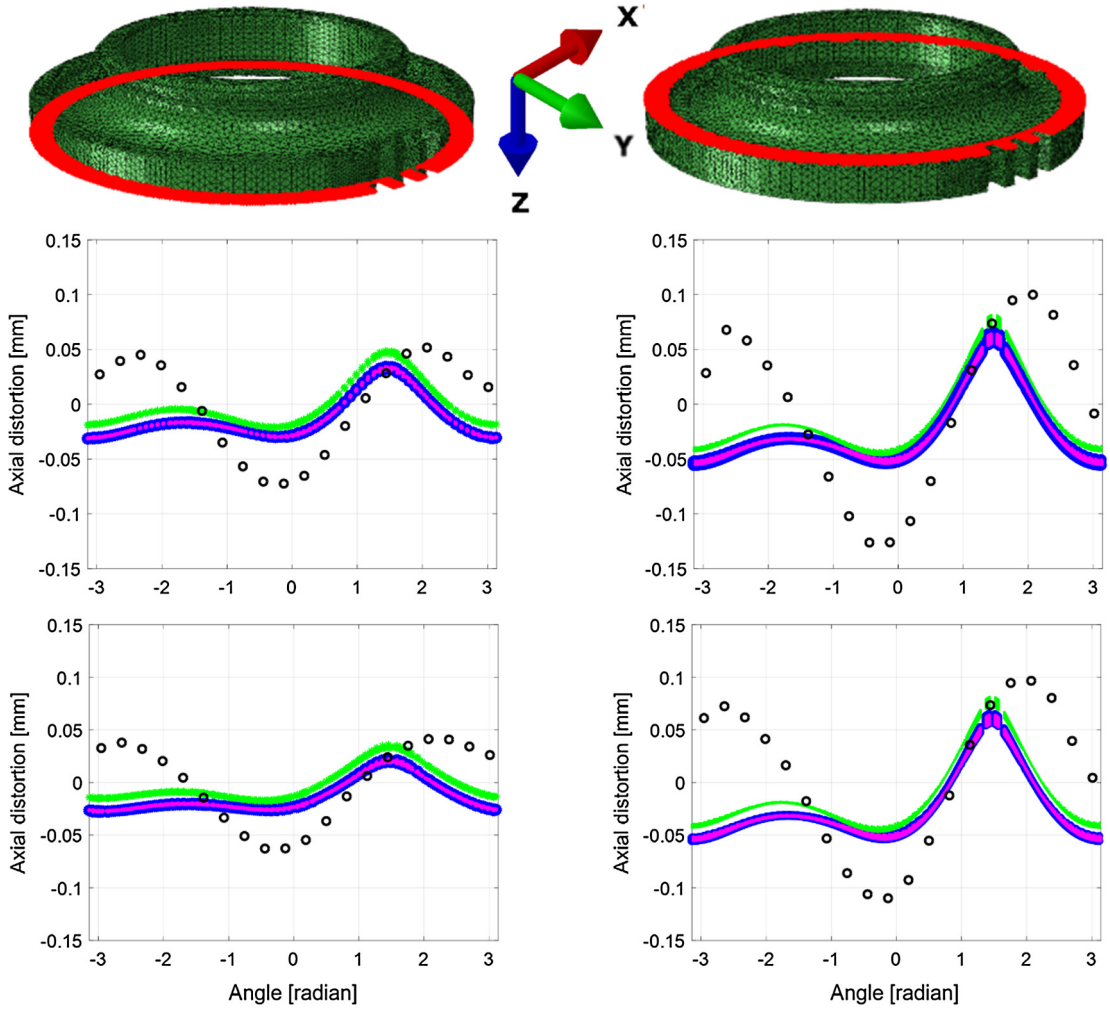

Fig. 9. Comparison of CMM (discrete symbols) measurements and predicted axial distortion for the top (on the left) and the bottom (on the right) surfaces of the rim portion of the disk at two radial locations: close to the outside (upper plots) and close to the inside (lower plots). The legend is the same as in Fig. 8. The highlighted nodes show the inspected surfaces by CMM, where the measurements are recorded at 20 points i.e. every 18° circumferentially for a given radius.

after the turning operation when the disk is in the unclamped state) for the outer and inner diameters. The plots are made as a function of the angular position. The predictions based on the three elastic stiffness tensors are presented. The incremental radial distortion was measured at 20 clock positions as well as at several locations along the height (i.e. the Z direction). Fig. 8 shows the comparison for near the top and bottom vertical locations. While the order of magnitude and trends can be regarded as being captured well by the model, the discrepancy in the actual values is evident. Possible sources of the error will be discussed shortly.

Fig. 9 shows a comparison between the predicted and measured axial distortion for the top and bottom surface at two radial locations. Axial distortion was measured using CMM at several radial locations and at 20 clock positions. The comparison is made for each of the three elastic stiffness tensors. The location of the distinct sharp kink in the results is the location of the slots, as marked in Fig. 8. Again, while the order of magnitude and trends can be regarded as being captured well by the model, the discrepancy in the actual values is evident.

The machining distortion calculations demonstrate the utility of the automated procedure developed in this work for making multiple cuts. As indicated above, the predictions are reasonable. If the objective of the work was to accurately predict the distortion, then the following sources of the error in the initial stress, elastic stiffness tensor, and CMM data would have to be minimized. Part distortion prediction because of material removal processes and concurrent evolution of stress towards equilibrium depends strongly on the state and magnitude of the initial stress. Thus, prior thermo-mechanical process modeling must be accurate. The material properties governing thermal and mechanical response of the material play a major role in determining the initial stress. In contrast, the elastic properties are the main variable in the distortion simulations, but appear to have little impact for the subset of anisotropy for the case explored in this paper. There are challenges in acquiring accurate CMM data. The data is usually a cloud of points that need interpretation for a reference point. Finally, the numerical approach can result in some errors due to boundary conditions, mesh resolution, and interpolation after remeshing, which we can minimize by appropriate mesh size design.

4. Conclusions

In this paper, we have developed an automated procedure for the creation of complex geometries by using one or more Boolean cuts and subsequent finite element mesh generation. The procedure relies on the Boolean geometric operation in Abaqus software and scripting in Python, Patran, and Matlab. The single cut procedure was successfully applied for creating explicit grain structure finite element models of a micro-pillar and a micro-tube to facilitate full-field crystal plasticity modeling. Furthermore, the proce-

dure was applied to making multiple cuts from a single object while attaining the state of stress equilibrium after each cut. To this end, the distortion due to material removal in the presence of bulk residual stresses was simulated. The starting material for machining had a distribution of bulk residual stresses resulting from prior thermo-mechanical processing. Machining of the disk by broaching and turning operations while predicting the distortion during and after cutting was carried out using the procedure. Automated start-to-finish runs of these simulation cases along with the predicted trends in distortion demonstrate the robustness and utility of the developed procedure.

Acknowledgements

This work is based upon a project supported by the U.S. National Science Foundation under grant no. CMMI-1650641. The authors gratefully acknowledge this support. D.J.S. acknowledges support through the National Science Foundation graduate research fellowship program.

Appendix A

This appendix presents values of the elastic stiffness tension components in MPa for IN718 used in the FE simulations of machining distortion. The single crystal elastic constants for IN718 needed for the elastic stiffness tensor calculations of $\{0\,0\,1\}$ and $\{0\,1\,1\}$ fiber textures were: $C_{11} = 242,180$MPa, $C_{12} = 138,850$MPa, and $C_{44} = 104,200$MPa [98], while Young's modulus and Poisson's ratio for the isotropic material were: 200,000 MPa and 0.3, respectively [90,99].

C [MPa]	Isotropic	$\{0\,0\,1\}$ fiber texture	$\{0\,1\,1\}$ fiber texture
C_{1111}	269,720	278,557	285,967
C_{1122}	115,590	116,044	118,050
C_{1133}	115,590	125,279	115,863
C_{1112}	0	238	−40
C_{1113}	0	1214	114
C_{1123}	0	912	1
C_{2222}	269,720	280,649	285,963
C_{2233}	115,590	123,187	115,867
C_{2212}	0	−159	35
C_{2213}	0	371	−13
C_{2223}	0	1567	−117
C_{3333}	269,720	271,414	288,150
C_{3312}	0	−79	5
C_{3313}	0	−1586	−101
C_{3323}	0	−2478	116
C_{1212}	77,060	81,394	83,400
C_{1213}	0	912	1
C_{1223}	0	371	−13
C_{1313}	77,060	90,629	81,213
C_{1323}	0	−79	5
C_{2323}	77,060	88,537	81,217

References

[1] D. Peirce, R.J. Asaro, A. Needleman, An analysis of nonuniform and localized deformation in ductile single crystals, Acta Metall. 30 (1982) 1087–1119.
[2] O. Diard, S. Leclercq, G. Rousselier, G. Cailletaud, Distribution of normal stress at grain boundaries in multicrystals: application to an intergranular damage modeling, Comput. Mater. Sci. 25 (2002) 73–84.
[3] M. Jahedi, M. Ardeljan, I.J. Beyerlein, M.H. Paydar, M. Knezevic, Enhancement of orientation gradients during simple shear deformation by application of simple compression, J. Appl. Phys. 117 (2015) 214309.
[4] M. Ardeljan, R.J. McCabe, I.J. Beyerlein, M. Knezevic, Explicit incorporation of deformation twins into crystal plasticity finite element models, Comput. Methods Appl. Mech. Eng. 295 (2015) 396–413.
[5] Z. Zhao, M. Ramesh, D. Raabe, A.M. Cuitiño, R. Radovitzky, Investigation of three-dimensional aspects of grain-scale plastic surface deformation of an aluminum oligocrystal, Int. J. Plast. 24 (2008) 2278–2297.
[6] H. Lim, J.D. Carroll, C.C. Battaile, T.E. Buchheit, B.L. Boyce, C.R. Weinberger, Grain-scale experimental validation of crystal plasticity finite element simulations of tantalum oligocrystals, Int. J. Plast. 60 (2014) 1–18.
[7] M. Zecevic, R.J. McCabe, M. Knezevic, A new implementation of the spectral crystal plasticity framework in implicit finite elements, Mech. Mater. 84 (2015) 114–126.
[8] M. Zecevic, M. Knezevic, Modeling of Sheet Metal Forming Based on Implicit Embedding of the Elasto-Plastic Self-Consistent Formulation in Shell Elements: Application to Cup Drawing of AA6022-T4, JOM 69 (2017) 922–929.
[9] M. Ardeljan, I.J. Beyerlein, B.A. McWilliams, M. Knezevic, Strain rate and temperature sensitive multi-level crystal plasticity model for large plastic deformation behavior: application to AZ31 magnesium alloy, Int. J. Plast. 83 (2016) 90–109.
[10] M. Zecevic, I.J. Beyerlein, R.J. McCabe, B.A. McWilliams, M. Knezevic, Transitioning rate sensitivities across multiple length scales: microstructure-property relationships in the Taylor cylinder impact test on zirconium, Int. J. Plast. 84 (2016) 138–159.
[11] M. Zecevic, M. Knezevic, I.J. Beyerlein, R.J. McCabe, Texture formation in orthorhombic alpha-uranium under simple compression and rolling to high strains, J. Nucl. Mater. 473 (2016) 143–156.
[12] D.J. Savage, I.J. Beyerlein, M. Knezevic, Coupled texture and non-Schmid effects on yield surfaces of body-centered cubic polycrystals predicted by a crystal plasticity finite element approach, Int. J. Solids Struct. 109 (2017) 22–32.
[13] M. Knezevic, J. Crapps, I.J. Beyerlein, D.R. Coughlin, K.D. Clarke, R.J. McCabe, Anisotropic modeling of structural components using embedded crystal plasticity constructive laws within finite elements, Int. J. Mech. Sci. 105 (2016) 227–238.
[14] T. Mura, Micromechanics of Defects in Solids, second ed., Martinus Nijhoff Publishers, Netherlands, 1987.
[15] H. Moulinec, P. Suquet, A numerical method for computing the overall response of nonlinear composites with complex microstructure, Comput. Methods Appl. Mech. Eng. 157 (1998) 69–94.
[16] R. Lebensohn, N-site modeling of a 3D viscoplastic polycrystal using fast Fourier transform, Acta Mater. 49 (2001) 2723–2737.
[17] B. Liu, D. Raabe, F. Roters, P. Eisenlohr, R.A. Lebensohn, Comparison of finite element and fast Fourier transform crystal plasticity solvers for texture prediction, Modell. Simul. Mater. Sci. Eng. 18 (2010) 085005.
[18] R.A. Lebensohn, R. Brenner, O. Castelnau, A.D. Rollett, Orientation image-based micromechanical modelling of subgrain texture evolution in polycrystalline copper, Acta Mater. 56 (2008) 3914–3926.
[19] A. Eghtesad, M. Zecevic, R.A. Lebensohn, R.J. McCabe, M. Knezevic, Spectral database constitutive representation within a spectral micromechanical solver for computationally efficient polycrystal plasticity modelling, Comput. Mech. 1–16 (2017).
[20] G.I. Taylor, Plastic strain in metals, J. Inst. Met. 62 (1938) 307–324.
[21] R.A. Lebensohn, C.N. Tomé, A self-consistent anisotropic approach for the simulation of plastic deformation and texture development of polycrystals: application to zirconium alloys, Acta Metall. Mater. 41 (1993) 2611–2624.
[22] R.A. Lebensohn, M. Zecevic, M. Knezevic, R.J. McCabe, Average intragranular misorientation trends in polycrystalline materials predicted by a viscoplastic self-consistent approach, Acta Mater. 104 (2016) 228–236.
[23] M. Zecevic, W. Pantleon, R.A. Lebensohn, R.J. McCabe, M. Knezevic, Predicting intragranular misorientation distributions in polycrystalline metals using the viscoplastic self-consistent formulation, Acta Mater. 140 (2017) 398–410.
[24] M. Knezevic, S.R. Kalidindi, D. Fullwood, Computationally efficient database and spectral interpolation for fully plastic Taylor-type crystal plasticity calculations of face-centered cubic polycrystals, Int. J. Plast. 24 (2008) 1264–1276.
[25] M. Knezevic, H.F. Al-Harbi, S.R. Kalidindi, Crystal plasticity simulations using discrete Fourier transforms, Acta Mater. 57 (2009) 1777–1784.
[26] M. Zecevic, M. Knezevic, I.J. Beyerlein, R.J. McCabe, Origin of texture development in orthorhombic uranium, Mater. Sci. Eng. A 665 (2016) 108–124.
[27] M. Knezevic, J.S. Carpenter, M.L. Lovato, R.J. McCabe, Deformation behavior of the cobalt-based superalloy Haynes 25: experimental characterization and crystal plasticity modeling, Acta Mater. 63 (2014) 162–168.
[28] M. Knezevic, I.J. Beyerlein, M.L. Lovato, C.N. Tomé, A.W. Richards, R.J. McCabe, A strain-rate and temperature dependent constitutive model for BCC metals incorporating non-Schmid effects: application to tantalum–tungsten alloys, Int. J. Plast. 62 (2014) 93–104.
[29] M. Knezevic, L. Capolungo, C.N. Tomé, R.A. Lebensohn, D.J. Alexander, B. Mihaila, R.J. McCabe, Anisotropic stress-strain response and microstructure evolution of textured α-uranium, Acta Mater. 60 (2012) 702–715.
[30] M. Knezevic, T. Nizolek, M. Ardeljan, I.J. Beyerlein, N.A. Mara, T.M. Pollock, Texture evolution in two-phase Zr/Nb lamellar composites during accumulative roll bonding, Int. J. Plast. 57 (2014) 16–28.
[31] M. Knezevic, D.J. Savage, A high-performance computational framework for fast crystal plasticity simulations, Comput. Mater. Sci. 83 (2014) 101–106.
[32] M. Knezevic, M. Zecevic, I.J. Beyerlein, R.A. Lebensohn, A numerical procedure enabling accurate descriptions of strain rate-sensitive flow of polycrystals

within crystal visco-plasticity theory, Comput. Methods Appl. Mech. Eng. 308 (2016) 468–482.
[33] M. Knezevic, A. Levinson, R. Harris, R.K. Mishra, R.D. Doherty, S.R. Kalidindi, Deformation twinning in AZ31: influence on strain hardening and texture evolution, Acta Mater. 58 (2010) 6230–6242.
[34] S.R. Kalidindi, C.A. Bronkhorst, L. Anand, Crystallographic texture evolution in bulk deformation processing of FCC metals, J. Mech. Phys. Solids 40 (1992) 537–569.
[35] S.R. Kalidindi, H.K. Duvvuru, M. Knezevic, Spectral calibration of crystal plasticity models, Acta Mater. 54 (2006) 1795–1804.
[36] C. Miehe, J. Schröder, J. Schotte, Computational homogenization analysis in finite plasticity Simulation of texture development in polycrystalline materials, Comput. Methods Appl. Mech. Eng. 171 (1999) 387–418.
[37] A.J. Beaudoin, P.R. Dawson, K.K. Mathur, U.F. Kocks, D.A. Korzekwa, Application of polycrystal plasticity to sheet forming, Comput. Methods Appl. Mech. Eng. 117 (1994) 49–70.
[38] G.B. Sarma, P.R. Dawson, Texture predictions using a polycrystal plasticity model incorporating neighbor interactions, Int. J. Plast. 12 (1996) 1023–1054.
[39] M. Ardeljan, I.J. Beyerlein, M. Knezevic, A dislocation density based crystal plasticity finite element model: application to a two-phase polycrystalline HCP/BCC composites, J. Mech. Phys. Solids 66 (2014) 16–31.
[40] G.B. Sarma, P.R. Dawson, Effects of interactions among crystals on the inhomogeneous deformations of polycrystals, Acta Mater. 44 (1996) 1937–1953.
[41] D.P. Mika, P.R. Dawson, Effects of grain interaction on deformation in polycrystals, Mater. Sci. Eng. A 257 (1998) 62–76.
[42] L. Delannay, P.J. Jacques, S.R. Kalidindi, Finite element modeling of crystal plasticity with grains shaped as truncated octahedrons, Int. J. Plast. 22 (2006) 1879–1898.
[43] H. Ritz, P. Dawson, Sensitivity to grain discretization of the simulated crystal stress distributions in FCC polycrystals, Modell. Simulat. Mater. Sci. Eng. 17 (2008) 015001.
[44] S.R. Kalidindi, A. Bhattacharya, R. Doherty, Detailed analysis of plastic deformation in columnar polycrystalline aluminum using orientation image mapping and crystal plasticity models, Proc. R. Soc. Lond.: Math. Phys. Eng. Sci. 460 (2004) 1935–1956.
[45] O. Diard, S. Leclercq, G. Rousselier, G. Cailletaud, Evaluation of finite element based analysis of 3D multicrystalline aggregates plasticity: application to crystal plasticity model identification and the study of stress and strain fields near grain boundaries, Int. J. Plast. 21 (2005) 691–722.
[46] M. Shenoy, Y. Tjiptowidjojo, D. McDowell, Microstructure-sensitive modeling of polycrystalline IN 100, Int. J. Plast. 24 (2008) 1694–1730.
[47] M. Ardeljan, D.J. Savage, A. Kumar, I.J. Beyerlein, M. Knezevic, The plasticity of highly oriented nano-layered Zr/Nb composites, Acta Mater. 115 (2016) 189–203.
[48] M. De Berg, M. Van Kreveld, M. Overmars, O.C. Schwarzkopf, Computational Geometry, Springer, 2000.
[49] P. Zhang, M. Karimpour, D. Balint, J. Lin, Three-dimensional virtual grain structure generation with grain size control, Mech. Mater. 55 (2012) 89–101.
[50] B. Boots, The arrangement of cells in "random" networks, Metallography 15 (1982) 53–62.
[51] D. Aboav, The arrangement of grains in a polycrystal, Metallography 3 (1970) 383–390.
[52] DREAM.3D Version 4.2, BlueQuartz Software, Springboro, OH, USA, 2013.
[53] M.A. Groeber, M.A. Jackson, DREAM. 3D: A digital representation environment for the analysis of microstructure in 3D, Integr. Mater. Manuf. Innov. 3 (2014) 5.
[54] M. Groeber, S. Ghosh, M.D. Uchic, D.M. Dimiduk, A framework for automated analysis and simulation of 3D polycrystalline microstructures. Part 2: Synthetic structure generation, Acta Mater. 56 (2008) 1274–1287.
[55] M. Knezevic, B. Drach, M. Ardeljan, I.J. Beyerlein, Three dimensional predictions of grain scale plasticity and grain boundaries using crystal plasticity finite element models, Comput. Methods Appl. Mech. Eng. 277 (2014) 239–259.
[56] M. Ardeljan, M. Knezevic, T. Nizolek, I.J. Beyerlein, N.A. Mara, T.M. Pollock, A study of microstructure-driven strain localizations in two-phase polycrystalline HCP/BCC composites using a multi-scale model, Int. J. Plast. 74 (2015) 35–57.
[57] J.E. Spowart, H.E. Mullens, B.T. Puchala, Collecting and analyzing microstructures in three dimensions: a fully automated approach, JOM 55 (2003) 35–37.
[58] J.E. Spowart, Automated serial sectioning for 3-D analysis of microstructures, Scr. Mater. 55 (2006) 5–10.
[59] N. Zaafarani, D. Raabe, R. Singh, F. Roters, S. Zaefferer, Three-dimensional investigation of the texture and microstructure below a nanoindent in a Cu single crystal using 3D EBSD and crystal plasticity finite element simulations, Acta Mater. 54 (2006) 1863–1876.
[60] M. Calcagnotto, D. Ponge, E. Demir, D. Raabe, Orientation gradients and geometrically necessary dislocations in ultrafine grained dual-phase steels studied by 2D and 3D EBSD, Mater. Sci. Eng. A 527 (2010) 2738–2746.
[61] A. Khorashadizadeh, D. Raabe, S. Zaefferer, G. Rohrer, A. Rollett, M. Winning, Five-parameter grain boundary analysis by 3D EBSD of an ultra fine grained Cuzr alloy processed by equal channel angular pressing, Adv. Eng. Mater. 13 (2011) 237–244.
[62] S. Zaefferer, S. Wright, D. Raabe, Three-dimensional orientation microscopy in a focused ion beam–scanning electron microscope: a new dimension of microstructure characterization, Metall. Mater. Trans. A 39 (2008) 374–389.
[63] S. Yi, I. Schestakow, S. Zaefferer, Twinning-related microstructural evolution during hot rolling and subsequent annealing of pure magnesium, Mater. Sci. Eng. A 516 (2009) 58–64.
[64] M.D. Uchic, M.A. Groeber, D.M. Dimiduk, J.P. Simmons, 3D microstructural characterization of nickel superalloys via serial-sectioning using a dual beam FIB-SEM, Scr. Mater. 55 (2006) 23–28.
[65] S.F. Li, J. Lind, C.M. Hefferan, R. Pokharel, U. Lienert, A.D. Rollett, R.M. Suter, Three-dimensional plastic response in polycrystalline copper via near-field high-energy X-ray diffraction microscopy, J. Appl. Crystallogr. 45 (2012) 1098–1108.
[66] J. Lind, S.F. Li, R. Pokharel, U. Lienert, A.D. Rollett, R.M. Suter, Tensile twin nucleation events coupled to neighboring slip observed in three dimensions, Acta Mater. 76 (2014) 213–220.
[67] C.A. Stein, A. Cerrone, T. Ozturk, S. Lee, P. Kenesei, H. Tucker, R. Pokharel, J. Lind, C. Hefferan, R.M. Suter, A.R. Ingraffea, A.D. Rollett, Fatigue crack initiation, slip localization and twin boundaries in a nickel-based superalloy, Curr. Opin. Solid State Mater. Sci. 18 (2014) 244–252.
[68] W. Ludwig, S. Schmidt, E.M. Lauridsen, H.F. Poulsen, X-ray diffraction contrast tomography: a novel technique for three-dimensional grain mapping of polycrystals. I. Direct beam case, J. Appl. Crystallogr. 41 (2008) 302–309.
[69] G. Johnson, A. King, M.G. Honnicke, J. Marrow, W. Ludwig, X-ray diffraction contrast tomography: a novel technique for three-dimensional grain mapping of polycrystals. II. The combined case, J. Appl. Crystallogr. 41 (2008) 310–318.
[70] L.-Q. Chen, Phase-field models for microstructure evolution, Annu. Rev. Mater. Res. 32 (2002) 113–140.
[71] A. Rollett, D. Raabe, A hybrid model for mesoscopic simulation of recrystallization, Comput. Mater. Sci. 21 (2001) 69–78.
[72] A.D. Rollett, Overview of modeling and simulation of recrystallization, Prog. Mater. Sci. 42 (1997) 79–99.
[73] D. Raabe, Introduction of a scalable three-dimensional cellular automaton with a probabilistic switching rule for the discrete mesoscale simulation of recrystallization phenomena, Philos. Mag. A 79 (1999) 2339–2358.
[74] V. Marx, F.R. Reher, G. Gottstein, Simulation of primary recrystallization using a modified three-dimensional cellular automaton, Acta Mater. 47 (1999) 1219–1230.
[75] A.C. Lewis, A.B. Geltmacher, Image-based modeling of the response of experimental 3D microstructures to mechanical loading, Scr. Mater. 55 (2006) 81–85.
[76] S.M. Qidwai, D.M. Turner, S.R. Niezgoda, A.C. Lewis, A.B. Geltmacher, D.J. Rowenhorst, S.R. Kalidindi, Estimating the response of polycrystalline materials using sets of weighted statistical volume elements, Acta Mater. 60 (2012) 5284–5299.
[77] M. Zecevic, I.J. Beyerlein, M. Knezevic, Coupling elasto-plastic self-consistent crystal plasticity and implicit finite elements: Applications to compression, cyclic tension-compression, and bending to large strains, Int. J. Plast. 93 (2017) 187–211.
[78] M. Diehl, M. Groeber, C. Haase, D.A. Molodov, F. Roters, D. Raabe, Identifying structure-property relationships through DREAM.3D representative volume elements and DAMASK crystal plasticity simulations: an integrated computational materials engineering approach, JOM 69 (2017) 848–855.
[79] M. Zecevic, R.J. McCabe, M. Knezevic, Spectral database solutions to elasto-viscoplasticity within finite elements: application to a cobalt-based FCC superalloy, Int. J. Plast. 70 (2015) 151–165.
[80] S. Wang, W. Zhuang, J. Cao, J. Lin, An investigation of springback scatter in forming ultra-thin metal-sheet channel parts using crystal plasticity FE analysis, Int. J. Adv. Manuf. Technol. 47 (2010) 845–852.
[81] W. Zhuang, S. Wang, J. Cao, J. Lin, C. Hartl, Modelling of localised thinning features in the hydroforming of micro-tubes using the crystal-plasticity FE method, Int. J. Adv. Manuf. Technol. 47 (2010) 859–865.
[82] L. Liu, J. Sun, W. Chen, J. Zhang, Finite element analysis of machining processes of turbine disk of Inconel 718 high-temperature wrought alloy based on the theorem of minimum potential energy, Int. J. Adv. Manuf. Technol. 88 (2017) 3357–3369.
[83] M. Knezevic, B.K. Chun, J.Y. Oh, W.T. Wu, R.A. Ress Iii, M.G. Glavicic, S. Srivatsa, Modeling machining distortion using the finite element method:, Appl. Engine Disk 40 (2012) 40–46.
[84] C.R. Liu, Y.B. Guo, Finite element analysis of the effect of sequential cuts and tool–chip friction on residual stresses in a machined layer, Int. J. Mech. Sci. 42 (2000) 1069–1086.
[85] T.D. Marusich, S. Usui, K.J. Marusich, Finite Element Modeling of Part Distortion, in: C. Xiong, H. Liu, Y. Huang, Y. Xiong (Eds.), Intelligent Robotics and Applications: First International Conference, ICIRA 2008 Wuhan, China, October 15–17, 2008, Proceedings, Part II, Springer, Berlin Heidelberg, 2008, pp. 329–338.
[86] H. Guo, D.W. Zuo, H.B. Wu, F. Xu, G.Q. Tong, Prediction on milling distortion for aero-multi-frame parts, Mater. Sci. Eng. A 499 (2009) 230–233.
[87] S. Masoudi, S. Amini, E. Saeidi, H. Eslami-Chalander, Effect of machining-induced residual stress on the distortion of thin-walled parts, Int. J. Adv. Manuf. Technol. 76 (2015) 597–608.
[88] Patran Version, MSC Software Corporation, Newport Beach, CA, USA, 2013.
[89] ABAQUS Version 6, Dassault Systèmes, Providence, RI, USA, 2017.

[90] D.H. Smith, J. Bicknell, L. Jorgensen, B.M. Patterson, N.L. Cordes, I. Tsukrov, M. Knezevic, Microstructure and mechanical behavior of direct metal laser sintered Inconel alloy 718, Mater. Charact. 113 (2016) 1–9.
[91] S. Gribbin, J. Bicknell, L. Jorgensen, I. Tsukrov, M. Knezevic, Low cycle fatigue behavior of direct metal laser sintered Inconel alloy 718, Int. J. Fatigue 93 (Part 1) (2016) 156–167.
[92] S. Ghorbanpour, M. Zecevic, A. Kumar, M. Jahedi, J. Bicknell, L. Jorgensen, I.J. Beyerlein, M. Knezevic, A crystal plasticity model incorporating the effects of precipitates in superalloys: application to tensile, compressive, and cyclic deformation of Inconel 718, Int. J. Plast., 2017.
[93] R. Hill, The elastic behavior of a crystalline aggregate, Proc. R. Soc. Lond. Ser. A Math. Phys. Sci. 65 (1952) 349–354.
[94] M. Knezevic, S.R. Kalidindi, Fast computation of first-order elastic-plastic closures for polycrystalline cubic-orthorhombic microstructures, Comput. Mater. Sci. 39 (2007) 643–648.
[95] N. Landry, M. Knezevic, Delineation of first-order elastic property closures for hexagonal metals using fast Fourier transforms, Materials 8 (2015) 6326–6345.
[96] S.R. Kalidindi, M. Knezevic, S. Niezgoda, J. Shaffer, Representation of the orientation distribution function and computation of first-order elastic properties closures using discrete Fourier transforms, Acta Mater. 57 (2009) 3916–3923.
[97] T. Fast, M. Knezevic, S.R. Kalidindi, Application of microstructure sensitive design to structural components produced from hexagonal polycrystalline metals, Comput. Mater. Sci. 43 (2008) 374–383.
[98] P. Haldipur, Material characterization of nickel-based super alloys through ultrasonic inspection, Materials Science and Engineering, Iowa State University, Ames, Iowa, 2006.
[99] Inconel alloy 718, Special Metals Corporation, 2007.